Phase transitions and potential ferroelectricity in noncentrosymmetric $KNaNbOF_5$

Jaye K. Harada,[1] Po-Hsiu Chien,[2,*] Haoyu Liu,[2] Sawankumar Patel,[2] Ching-Hwa A. Chen,[3] Nenian Charles,[4] Yan-Yan Hu,[2,5] Kenneth R. Poeppelmeier,[1,3] and James M. Rondinelli[1,†]

[1]*Department of Materials Science and Engineering, Northwestern University, Evanston, Illinois 60208, USA*
[2]*Department of Chemistry and Biochemistry, Florida State University, Tallahassee, Florida 32306, USA*
[3]*Department of Chemistry, Northwestern University, Evanston, Illinois 60208, USA*
[4]*Department of Materials Science and Engineering, Drexel University, Philadelphia, Pennsylvania 19104, USA*
[5]*Center of Interdisciplinary Magnetic Resonance, National High Magnetic Field Laboratory, Tallahassee, Florida 32310, USA*

(Received 2 August 2021; accepted 10 November 2021; published 1 December 2021)

Increasing the number of known ferroelectrics requires expanding the chemical design space and mechanisms producing ferroelectricity. To that end, we examine the displacive, noncentrosymmetric-to-centrosymmetric phase transition in the oxyfluoride $KNaNbOF_5$ using *ab initio* calculations and Landau theory. We predict an intermediate *Pnma* phase occurs in the transition from the known low- and high-temperature phases, $Pna2_1$ and *Cmcm*, respectively, which we subsequently confirm using high-resolution and *in situ* ^{19}F magic-angle spinning nuclear magnetic resonance. Using the intermediate structure, we then calculate the monodomain polarization switching barrier in $KNaNbOF_5$ to be ∼93 meV per formula unit, comparable to existing ferroelectrics. The reversal of the polarization is due to uncompensated antipolar displacements of oxygen and fluorine and does not require oxygen and fluorine site exchange as in other nonswitchable heteroanionic materials, which makes $KNaNbOF_5$ a viable oxyfluoride for a switchable electric polarization.

DOI: 10.1103/PhysRevMaterials.5.124401

I. INTRODUCTION

A ferroelectric material requires a spontaneous polarization under zero applied electric field and the polarization must be "switchable," meaning the material can switch between different polarization states through an applied electric field [1]. Other technologically relevant properties such as piezoelectricity and second-harmonic generation are also active in ferroelectric materials; however, they do not rely on a switchable electric polarization [2]. Strategies to design and synthesize new ferroelectrics have largely focused on producing polar off-centering displacements in ABO_3 perovskite and perovskite-derived structures. Common ferroelectrics such as $BaTiO_3$ rely on d^0 transition-metal B sites to induce polarity into the structure through a second-order Jahn-Teller (SOJT) mechanism; however, this restricts the B-site chemistry to select elements. Hybrid improper ferroelectricity allows for a wider chemistry and coupling to other properties, e.g., magnetism, as it relies on rotations and tilting of the BO_6 octahedra to drive polar A-site displacements [3–6].

Recent work has gone beyond traditional perovskite-type oxides and fluorides, and has shown polar and/or noncentrosymmetric (NCS) structures may be realized by controlled modification of the anion-sublattice composition and structure. Anion vacancy ordering combined with A-site chemical ordering has been used successfully to generate NCS $Ba_2YFeO_{5.5}$ and $(SrFeO_{2.5})_1/(CaFeO_{2.5})_1$ thin films and superlattices [7,8], respectively. Anion substitution alone can be used to create polar-building-block units within a structure and their directed assembly can stabilize compounds without inversion symmetry [9,10]. NCS anion-substituted compounds, which we refer to as heteroanionic materials (HAMs), however, are still relatively rare [11]. For that reason, there are few conclusively demonstrated ferroelectric HAMs. Ferroelectric oxynitrides have been studied and proposed as relaxor ferroelectrics with a switchable polarization [12–14], but to our knowledge there are no known switchable ferroelectric oxyfluorides. $Na_3MoO_3F_3$ has been proposed to be a ferroelectric [15], however, its field-polarization hysteresis loop neither saturates nor exhibits a region with a large change in concavity [16,17]. Upon our microscopic analysis of the polarization in $Na_3MoO_3F_3$, we find that it arises from aligned $[MoO_3F_3]^{6-}$ units. For polarization reversal, significant mass transport (i.e., 180° rotations of the all $[MoO_3F_3]^{6-}$ units) would be required, which is difficult to achieve. It would involve disassembling the structure and reconnecting it in a manner analogous to how the structure of zincblende is noncentrosymmetric and permits a static polarization but cannot be reversed. Thus, to find a ferroelectric oxyfluoride, we not only require a polar structure, but the electronic polarization must be switchable below the breakdown voltage of the material with small displacive distortions.

$KNaNbOF_5$ is one of these rare polar heteroanionic materials that is also polymorphic [18]. Its synthesis is environmentally conscious and nontoxic. $KNaNbOF_5$ has a low processing temperature and its synthesis takes place in water without requiring use of aqueous HF [19]. It exhibits

*Present address: Neutron Scattering Division, Oak Ridge National Laboratory, Oak Ridge, Tennessee 37831, USA.
†jrondinelli@northwestern.edu

a metastable centrosymmetric (CS) phase [20] and a polar structure at room temperature [19,21]. This polar ground-state structure has $Pna2_1$ symmetry and exhibits a reversible, temperature-driven phase transition to a high-temperature (HT) centrosymmetric (CS) phase with symmetry *Cmcm* [19,22], which makes it a potential switchable ferroelectric. Our analysis of the group-subgroup relationships for the HT and NCS phases, which we present in detail below, reveals that a complex phase transition with either proper or hybrid-improper character may occur depending on whether the relevant unstable modes driving the transition condense sequentially or simultaneously. If two or more modes condense together at the same temperature, $KNaNbOF_5$ would exhibit an unusual avalanche transition [3,23,24]. If the modes do not condense together, then an intermediate phase would appear, and the transition becomes proper. Ferroelectric switching could also be more likely, as the intermediate phase may provide for a lower-energy polarization reversal pathway.

Here we investigate ferroelectricity in $KNaNbOF_5$ by examining the sequence of possible phase transitions occurring between its ground-state NCS phase and its HT phase. We first investigate the character of possible phase transitions by constructing a Landau model using order parameters and interactions obtained from density functional theory (DFT) calculations. Our model suggests an intermediate phase with *Pnma* symmetry should appear between the previously identified HT and NCS phases. We then verify the existence of this phase experimentally using high-resolution and *in situ* ^{19}F magic-angle spinning (MAS) solid-state NMR, which finds that the intermediate phase likely exists between ∼360 °C and ∼380 °C. Furthermore, we show that the electric polarization in the compound arises from the antipolar displacements of oxygen and fluorine atoms. We also identify that a low-energy monodomain ferroelectric switching path occurs through this *Pnma* phase by reversal of these antipolar displacements. Our results suggest that $KNaNbOF_5$ is an ideal ferroelectric oxyfluoride candidate. We hope our results spur additional interest in oxyfluorides and heteroanionic materials, which have broad applications as functional electroceramics in ferroic-based devices, in linear and nonlinear optoelectronic devices, as phosphors for solid-state lighting, and in energy storage systems, among others [11,25,26].

II. METHODS

A. Computational details

All calculations were performed using density functional theory (DFT) as implemented in the Vienna *Ab initio* Simulation Package (VASP) [27,28]. We used the generalized gradient approximation of the exchange correlation functional of Perdew, Burke, and Ernzerhof revised for solids (PBEsol) [29] and the meta-GGA functional SCAN [30] as recommended by recent computational studies of oxyfluorides [31]. We also used projector augmented wave (PAW) potentials [32] with the following valence configurations: $3s^2 3p^6 4s^1$ for K, $2p^6 3s^1$ for Na, $4p^6 5s^2 4d^4$ for Nb, $2s^2 2p^4$ for O, and $2s^2 2p^5$ for F. A plane-wave cutoff of 600 eV and a $5 \times 3 \times 5$ Monkhorst-Pack mesh [33] were used for structure relaxations and total energy calculations. Structure relaxations were converged to have forces less than 1 meV Å^{-1} on each atom.

To investigate the energetics of the monodomain switching path, a generalized solid-state nudged elastic band (G-SSNEB) method was used [34]. Forces on ions in the G-SSNEB calculation were converged to less than 10 meV Å^{-1}. Phonon frequencies were calculated using the frozen phonon method with 0.03 Å displacements in $2 \times 2 \times 2$ supercells of the primitive cell. The PHONOPY software package [35] was used to calculate the force constants and dynamical matrices from the DFT calculations. Wannier centers and maximally localized Wannier functions were obtained using the WANNIER90 code [36]. The chemical shifts were determined by magnetic shieldings using perturbation theory (linear response) [37,38]. The calculated isotropic shifts, which included the contribution of $\mathbf{G} = 0$ and PAW cores, were then calibrated with a calibration factor of +15 ppm according to our previous work [39].

Crystallographic symmetry-adapted modes were analyzed using ISODISTORT [40]. The Landau free energy expansion was generated using the INVARIANTS tool [41]. In our analysis of the Landau free energy, we utilized the unstable phonon eigenvectors, which are obtained from the force constant matrices of the fully relaxed *Cmcm* structure. Under a given irrep, these modes are allowed to mix to form the symmetry-adapted basis. We used the eigenvectors because using the symmetry-adapted modes alone were found to be stable with the mode distortion. The symmetry-adapted modes and the details on the linear combination of these eigenvectors to fulfill the symmetry-adapted modes is described in Table S1 and Fig. S1 of the Supplemental Material (SM) [42]. Landau coefficients were obtained by a least-squares fit of a mesh of *ab initio* energy calculations to the Landau function. Quadratic coefficients were fit to at least 20 data points, biquadratic coefficients were fit to more than 400 points, and trilinear terms were fit to more than 1000 points.

B. Synthesis of $KNaNbOF_5$

Caution: Hydrofluoric acid is toxic and corrosive and must be handled with extreme caution and the appropriate protective gear. If contact with the liquid or vapor occurs, proper treatment procedures should immediately be followed [43–45].

The reagents NaF (99%, Aldrich), KNO_3 (99.9%, Mallinckrodt), Nb_2O_5 (99.5%, Strem), and aqueous hydrofluoric acid (HF) (48% HF by weight, Aldrich) were used as received. All reactants were sealed in Teflon pouches as previously described [46]. The precursor Na_2NbOF_5 was synthesized hydrothermally via a previously published procedure by combining 0.1344 g (3.20 mmol) NaF, 0.4254 g (1.60 mmol) Nb_2O_5, and 1.2 ml (60.0 mmol) aqueous HF in a Teflon pouch [19,22]. Six pouches were placed in a 125 ml Teflon-lined Parr pressure vessel filled with 42 ml deionized water as backfill, and heated at 5 °C per min to 150 °C, held for 24 h, and slowly cooled to room temperature at 5 °C per min. The cooled products were left in the pouches at room temperature to crystallize over two weeks. The product was recovered by vacuum filtration in air.

The $Pna2_1$ phase of $KNaNbOF_5$ was synthesized by combining 0.0496 g (0.198 mmol) Na_2NbOF_5, 0.0929 g (0.919 mmol) KNO_3, and 0.12 ml (6.7 mmol) deionized H_2O in a Teflon pouch [18]. Six pouches were placed in the Parr pressure vessel with 49 ml deionized water as backfill and heated at 5 °C per min to 150 °C, held for 24 h, and slowly cooled to room temperature at a slower rate of 1 °C per h. The pouches were then removed from the pressure vessel and left undisturbed at room temperature for 1–2 weeks. Crystals were recovered by vacuum filtration in air. Sample purity was confirmed by powder x-ray diffraction (PXRD) measurements on an Ultima IV x-ray diffractometer (Rigaku) with Cu K_α radiation from 10° to 60°. Careful readers will note that a similar synthesis with a lower K:Na ratio will produce the centrosymmetric polymorph of $KNaNbOF_5$. Additional details on successfully producing a phase pure sample of either polymorph is available in Ref. [19].

C. Characterization

The acquisition of *ex situ* ^{19}F magic-angle-spinning (MAS at 25 kHz) NMR spectra of $KNaNbOF_5$ (including as-synthesized $Pna2_1$, heated $Pna2_1$, and quenched samples as discussed below) was performed using the same experimental protocol as described previously [39]. *In situ* variable-temperature ^{19}F MAS NMR and ^{19}F T_1 relaxation time measurements were employed to track the displacive $Pna2_1$ (NCS) to *Cmcm* (HT) transition with a Bruker LAS-MAS probe [47]. Detailed experimental conditions (pulse sequence and pulsing parameters, heating/cooling control, etc.) are reported in Ref. [39]. After the *in situ* ^{19}F MAS NMR experiments, the heated sample was measured again with high-resolution ^{19}F MAS NMR experiments with an MAS rate of 25 kHz for postmortem phase identification.

To capture potential intermediate phases arising during the NCS-to-HT phase transition, as-synthesized NCS $KNaNbOF_5$ was heated to select temperatures (150 °C, 250 °C, 310 °C, and 360 °C) and quickly quenched in an ice bath (~0 °C). The as-synthesized NCS $KNaNbOF_5$ sample (~20 mg) was first placed in a ZrO_2 capsule, then loaded in a quartz tube and sealed under vacuum for quenching experiments. The tubes were then loaded into a tube furnace (Carbolite MTF 10/25/130) and held at the target temperature for 5 min before quenching. Then, the quenched samples were packed into 2.5 mm ZrO_2 rotors in a glove box (Mbraun Inc., H_2O <1 ppm, O_2 <1 ppm) for the ^{19}F MAS (25 kHz) NMR experiments. To describe the specific fluoride ions in the ^{19}F MAS NMR spectra of different phases of $KNaNbOF_5$, we use the notation: $F(\text{site number})_{\text{phase name}}$ throughout, e.g., $F1_{NCS}$, corresponds to the first crystallographic fluoride position in the NCS $Pna2_1$ structure.

We note that our starting material contains both the centrosymmetric perovskite-derived $P4/nmm$ phase and NCS phase, however, we are confident that we can distinguish the irreversible, reconstructive ($P4/nmm \rightarrow Cmcm$) from the reversible, displacive ($Pna2_1 \leftrightarrow Cmcm$) transitions given that these transitions have been studied using the same technique [39]. We show equivalent experimental results for the reconstructive phase transition and discuss their potential impacts on the results in the displacive phase transition in the Supplemental Material [42].

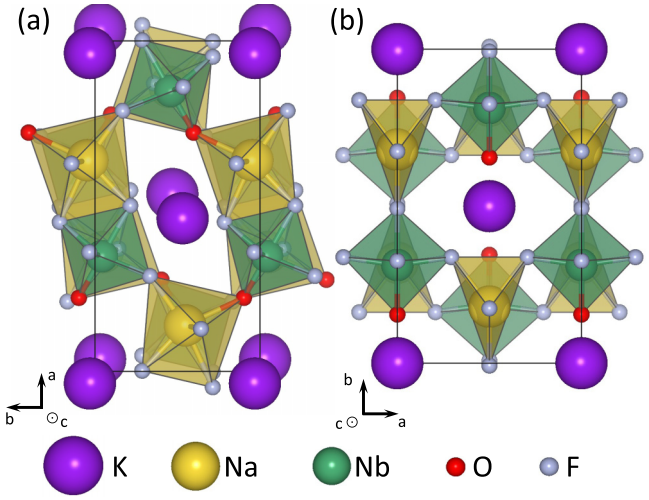

FIG. 1. The (a) $Pna2_1$ (NCS) and (b) *Cmcm* (HT) structures of $KNaNbOF_5$.

III. RESULTS AND DISCUSSION

A. Symmetry analysis and energetics

To understand the nature of the $Pna2_1$ to *Cmcm* phase transition in $KNaNbOF_5$, we first examine the relationship between the structures using a mode analysis [48,49]. For the analysis of the displacive motion of atoms that reduce the *Cmcm* structure to $Pna2_1$, we use the DFT optimized structures reported in Table S2. Although the HT structure exhibits corner-connecting heteroleptic and homoleptic units and the NCS structures exhibits only edge- and corner-connected heteroleptic units (Fig. 1), the transition between these distinct structures maintains a group-subgroup relationship.

Figure 2 shows the results of our symmetry analysis for the high-symmetry (*Cmcm*) to low-symmetry ($Pna2_1$) transition. Unlike a proper phase transition, which typically requires the condensation of only one mode, this transition requires the condensation of at least two (of a possible three) modes to obtain the $Pna2_1$ space group as shown in the group-subgroup tree [Fig. 2(a)]. Each symmetry mode presented displaces atoms according to a particular subgroup symmetry, which are labeled according to the irreducible representations (irreps) of the high-symmetry *Cmcm* phase. The modes are Y_2^+, Y_1^-, and Γ_2^-. Their corresponding atomic displacements, obtained from the lowest-frequency phonon eigenvectors of the *Cmcm* force constant matrices, are shown on the left of Fig. 2. The Y_2^+ mode is an out-of-phase rotation of the $[NbOF_5]^{2-}$ and $[NaF_5]^{4-}$ polyhedra about the *c* axis. The Y_1^- mode is an in-phase rotation of the polyhedra about the *b* axis, and the Γ_2^- mode induces polar displacements into the high-temperature structure, primarily through uncompensated antipolar displacements of the O^{2-} and F^- ions as denoted by the black arrows in Fig. 2. The polar mode also comprises large antipolar displacements of the K^+ ions along the *b* axis (black arrows).

Condensing these modes individually into the *Cmcm* structure shows their expected energy-lowering behavior

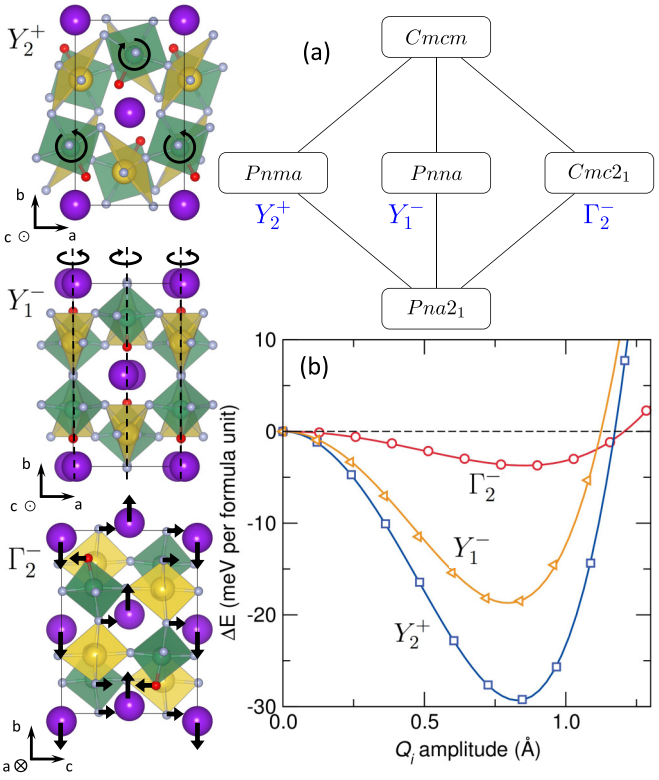

FIG. 2. Mode decomposition and energetics of $KNaNbOF_5$. (a) Group-subgroup relationship between the high- and low-temperature phases. The irreps associated with each intermediate structure are show in blue. (b) Energetics of each of the modes associated with the transition. The atomic displacements associated with the unstable modes from force constant eigenvectors, which transform as irreps indicated in blue, are also shown in the atomic structures on the left. Atoms are designated as in Fig. 1.

[Fig. 2(b)]. The Y_2^+ mode is the most unstable, with its minimum around an amplitude of 0.83 Å, and followed by Y_1^- with its minimum around 0.80 Å. The polar mode, Γ_2^- is the least energy stabilizing, exhibiting a shallow energy well at a slightly higher amplitude of 0.86 Å and depth of ≈ -3.72 meV per formula unit (f.u.). Based on these energetics, it is likely that the nonpolar modes transforming as Y_2^+ and Y_1^- drive the NCS-to-CS transition as they are considerably more unstable than the polar Γ_2^- mode.

B. Approximate *ab initio* phase diagram

To determine the character of this phase transition in $KNaNbOF_5$, we follow a procedure used to investigate the sequence of phase transitions in $SrBi_2Ta_2O_9$ and $SrBi_2Nb_2O_9$ [23], which also exhibits a complex energy landscape with multiple mode couplings. The approach involves computing the 0 K free energy Landau expansion using *ab initio* DFT energy calculations to obtain the coefficients for symmetry-permitted terms that involve the active order parameters and their coupled interactions. Based on this Landau model, an approximate phase diagram with variable quadratic coefficients is constructed to reveal whether a direct transition between the high- and low-symmetry phases are allowed.

Following this procedure, we first construct a zero-temperature energy model (ΔE_{0K}) using the relevant unstable modes, Y_2^+, Y_1^-, and Γ_2^-, for the transition as follows:

$$\Delta E_{0K} = E_i + E_{ij} + E_{ijk}. \tag{1}$$

The homogeneous terms (E_i) are

$$E_{\Gamma_2^-} = \alpha_{\Gamma_2^-} Q_{\Gamma_2^-}^2 + \beta_{\Gamma_2^-} Q_{\Gamma_2^-}^4,$$
$$E_{Y_2^+} = \alpha_{Y_2^+} Q_{Y_2^+}^2 + \beta_{Y_2^+} Q_{Y_2^+}^4,$$
$$E_{Y_1^-} = \alpha_{Y_1^-} Q_{Y_1^-}^2 + \beta_{Y_1^-} Q_{Y_1^-}^4,$$

and the biquadratic terms (E_{ij}) are

$$E_{\Gamma_2^- Y_2^+} = \delta_{\Gamma_2^- Y_2^+} Q_{\Gamma_2^-}^2 Q_{Y_2^+}^2,$$
$$E_{Y_2^+ Y_1^-} = \delta_{Y_2^+ Y_1^-} Q_{Y_2^+}^2 Q_{Y_1^-}^2,$$
$$E_{Y_1^- \Gamma_2^-} = \delta_{Y_1^- \Gamma_2^-} Q_{Y_1^-}^2 Q_{\Gamma_2^-}^2.$$

Last, the trilinear term (E_{ijk}) coupling each order parameter is

$$E_{\Gamma_2^- Y_2^+ Y_1^-} = \gamma_{\Gamma_2^- Y_2^+ Y_1^-} Q_{\Gamma_2^-} Q_{Y_2^+} Q_{Y_1^-}.$$

We now approximate the zero-temperature free energy of the system using coefficients for α, β, δ, and γ calculated from DFT at 0 K. Values for all coefficients are listed in Table S3. Using Eq. (1), we approximate the free energy under assumptions imposed by the Landau theory.[1] Then, the temperature renormalization is solely contained in the quadratic terms, such that $\alpha_i = a_i(T - T_{0,i})$ for a given mode i, where a_i is a constant and $T_{0,i}$ is the critical temperature. Under this approximation, the free energy is

$$F = \sum_i^3 \left[a_i(T - T_{0,i})Q_i^2 + \beta_i Q_i^4\right] + E_{\Gamma_2^- Y_2^+} + E_{Y_2^+ Y_1^-} + E_{Y_1^- \Gamma_2^-} + E_{\Gamma_2^- Y_2^+ Y_1^-}. \tag{2}$$

Because we are approximating a finite temperature system, the coefficients obtained from the fits to the *ab initio* data from the unstable eigenvectors are directly related to the stiffness coefficients and transition temperatures, $\alpha_{0,i} = -a_i T_{0,i}$. Given that the quadratic stiffness coefficient is linear with temperature, we can construct a phase diagram in a region near $\alpha_i = 0$ to predict if a continuous, direct phase transition is possible between the high-temperature *Cmcm* and ground-state $Pna2_1$ phases.

Figure 3 presents the phase diagram of our 0 K Landau model for the transition in the space of the two most negative stiffness constants transforming as Y_2^+ and Y_1^-. Presenting the phase diagram in a two-dimensional space with three potential stiffness coefficients, requires us to impose a constraint between one of the coefficients of these order parameters and the amplitude of Γ_2^-. The slice presented in Fig. 3 gives the

[1]The assumptions made for Landau theory are (i) the phase transition is continuous (i.e., second order, though we do note we do see two-phase coexistence in our experiments later), (ii) a mean-field model is used so no fluctuations in the order parameter are considered here, and (iii) entropy is mainly produced by the phonons rather than any configurational disorder.

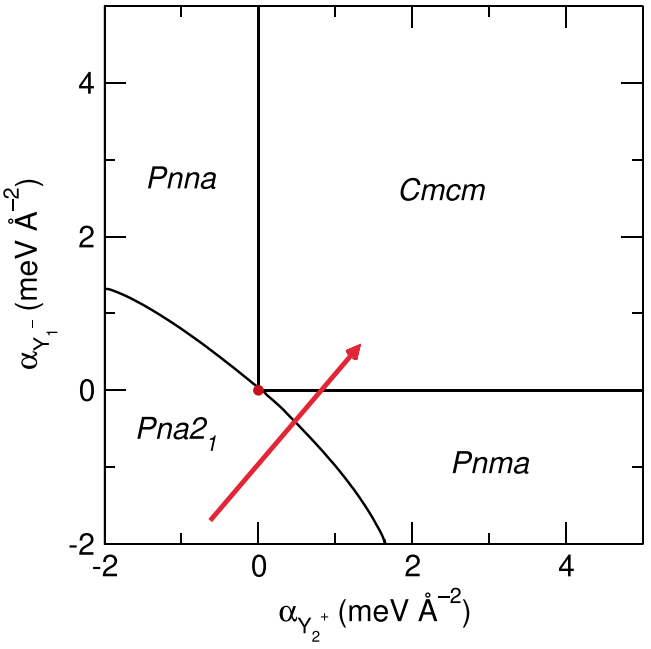

FIG. 3. Approximate phase diagram of the displacive transition in $KNaNbOF_5$ in which $\alpha_{\Gamma_2^-} = 0.6$ meV Å^{-2}. The red dot at (0,0) corresponds to the position in the phase diagram through which a direct transition between the high-temperature (*Cmcm*) and ground-state (*Pna*2$_1$) phases occurs. The red arrow represents a possible path of the phase transition through an intermediate centrosymmetric phase.

best case scenario for a direct phase transition between the HT and NCS phases, where $\alpha_{\Gamma_2^-} = 0.6$ meV Å^{-2}. Here we find a singular point at the origin, which allows for a direct phase transition between the phases. This scenario also exists under the following conditions: $0 < \alpha_{\Gamma_2^-} < 6$ meV Å^{-2}; $\alpha_{\Gamma_2^-} = \alpha_{Y_2^+} + n$ where $0 < n < 0.6$ meV Å^{-2}; and $\alpha_{\Gamma_2^-} = \alpha_{Y_1^-} + m$ where $0 < m < 0.6$ meV Å^{-2}. The only condition for this point to open and permit a direct transition between *Cmcm* and *Pna*2$_1$ is when the trilinear coupling coefficient is increased [Figs. S2(a), S2(b)], which is also seen in the case of $SrBi_2Ta_2O_9$ [23]. Given that we do not know the exact physical path the phase transition follows, we assume that a larger gap allowing a direct phase transition between the NCS and HT phases suggests that a direct transition is likely to occur. Because the gap between the phases is restricted to a singular point at the DFT-calculated trilinear coupling amplitude, we conclude that a hybrid-improper transition does not occur. The two unstable modes Y_2^+ and Y_1^- do not condense at the same temperature; therefore, an intermediate phase must exist to accommodate the transition between *Pna*2$_1$ and *Cmcm*. Given the single mode energetics in Fig. 2(b), we predict it to be one of the centrosymmetric phases: *Pnma* or *Pnna*. This makes the transition in $KNaNbOF_5$ a proper ferroelectric transition driven by the condensation of a single mode.

To confirm the absence of a direct transition gap in Fig. 3 is not functional or volume dependent, we repeat this procedure using the SCAN functional, which has been shown to give more accurate phonon frequencies in oxyfluoride materials [31]. Table S3 and Fig. S2(c) give the Landau coefficients and

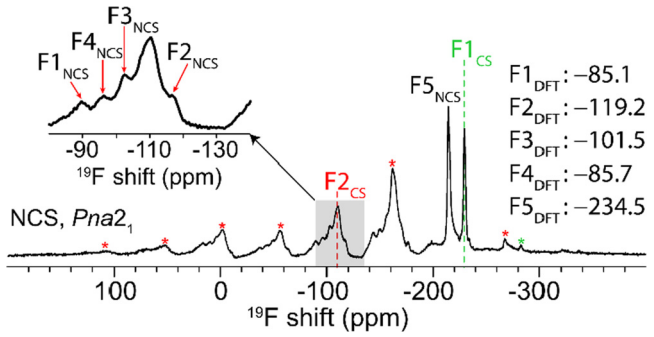

FIG. 4. High-resolution ^{19}F MAS (25 kHz) NMR spectrum of NCS *Pna*2$_1$ $KNaNbOF_5$ and its calculated ^{19}F NMR chemical shifts shown for reference. Asterisks (*) denote spinning side bands. ^{19}F MAS (25 kHz) NMR spectrum of CS *P*4/*nmm* $KNaNbOF_5$ is shown in Fig. S6 for comparison.

approximate phase diagram obtained using the SCAN functional, respectively. The trilinear coupling coefficient from the SCAN functional is slightly smaller than the PBEsol value (18.95 versus 20.17 meV Å^{-3}). As a result, the SCAN phase diagram is essentially identical to our PBEsol level diagram; there is a single point in which a direct transition can occur. Increasing the trilinear coupling coefficient is the only way to open passage between the *Pna*2$_1$ and *Cmcm* phases through a hybrid improper transition. Therefore, our conclusion remains the same and we expect an intermediate phase of either *Pnma* or *Pnna* symmetry, whose DFT relaxed structures and crystallographic information can be found in Figs. S3(b), S3(c), and Table S4. As described previously, the structures differ in the $[NbOF_5]^{-2}$ axis of rotation, which is about the *c* axis in *Pnma* and the *b* axis in *Pnna*. When the structures are relaxed, the *Pnma* structure is lowest in energy (93.3 and 282.2 meV per formula unit relative to *Pna*2$_1$, see Fig. S4).

C. *In situ* characterization of the transition

First, we confirm structure assignments of the *Pna*2$_1$ and *Cmcm* phases and the reversibility between these phases using *in situ* ^{19}F magic-angle-spinning (MAS) solid-state NMR. Previous experiments have shown the technique is able to distinguish among the known symmetries, *P*4/*nmm*, *Cmcm*, and *Pna*2$_1$ of $KNaNbOF_5$ [39]. Table S5 shows the calculated and observed isotropic chemical shifts of *Pna*2$_1$ and *Cmcm* and the proposed intermediate phases, *Pnma* and *Pnna*. Figure S3 shows the fluoride sites in the structures. Although it is difficult to resolve the equatorial fluoride sites, i.e., all fluoride sites that are not trans to the oxide in the $[NbOF_5]^{2-}$ octahedra, because of their close proximity in the ^{19}F NMR spectra, we can readily resolve the phases using the chemical shifts of the apical fluoride, i.e., the fluoride anion trans to the oxide anion. We also note that the apical fluoride anion is static throughout the phase transition (Fig. S5), indicating that there is no dynamic O/F disorder in the HT phase.

Figure 4 shows the high-resolution ^{19}F MAS (25 kHz) NMR spectrum of NCS *Pna*2$_1$ $KNaNbOF_5$. Among seven resolved ^{19}F resonances, we assign the peaks at −229.2 and −109.5 ppm to the fluoride anions F1$_{CS}$ and F2$_{CS}$,

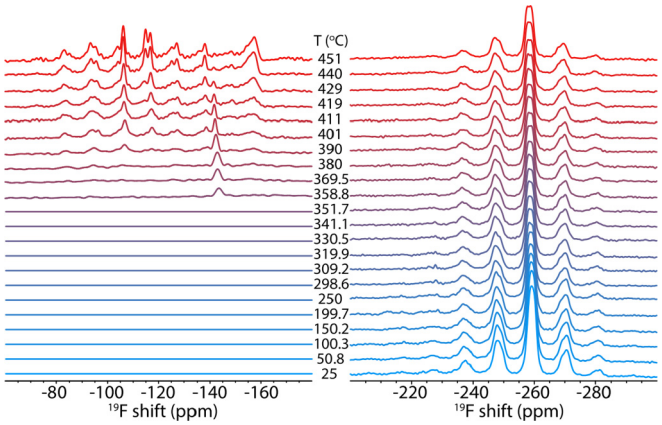

FIG. 5. *In situ* monitoring (heating process) of the phase transition in $KNaNbOF_5$ from the polar $Pna2_1$ to the high-temperature *Cmcm* phase by variable-temperature ^{19}F MAS (5 kHz) NMR.

respectively, of the CS $P4/nmm$ (perovskite-derived) phase of $KNaNbOF_5$ (see also Fig. S6). These assignments agree well with our previous results [39]. The remaining five ^{19}F chemical shifts at −89.8, −115.8, −100.1, −95.8, and from −214.2 ppm are assigned to the fluoride anions at sites $F1_{NCS}$ to $F5_{NCS}$ in the NCS phase. The isotropic shifts to which the F_{NCS} anions are assigned are verified by the calculated results from DFT (Table S5).

The $Pna2_1$ phase of $KNaNbOF_5$ exhibits five crystallographically distinct fluoride sites with no mixed occupancy; thus, the ratio among the five fluorine atoms is 1:1:1:1:1. In other words, the apical fluoride anion, $F5_{NCS}$, should ideally share 20% of the total ^{19}F integral in the NCS $KNaNbOF_5$ spectra. Experimentally, the percentage of the ^{19}F integral (including both isotropic shift and spinning side bands) of the apical fluorine anions $F5_{NCS}$ over the sum of all fluorine anions is 19.4%. The ratio among the equatorial fluorine anions ($F2_{NCS}$, $F3_{NCS}$, $F4_{NCS}$, and $F1_{NCS}$) is 1.02:0.83:1.13:1.15, which confirms the assignments of the ^{19}F resonances in the NCS phase.

Next, we performed *in situ* high-temperature ^{19}F MAS (5 kHz) NMR on the as-synthesized NCS $KNaNbOF_5$ to examine the reversibility of the $Pna2_1$ to *Cmcm* transition. The heating process is summarized in Fig. 5 and the cooling process is displayed in Fig. S7. From room temperature to ∼350 °C, no phase transition is observed. The only detectable ^{19}F resonance at −259.2 ppm is assigned to the apical fluoride anion, $F5_{NCS}$, in $KNaNbOF_5$ (Table S5 and Fig. S3). The ^{19}F signals for the equatorial fluoride anions in the NCS phase ($F2_{NCS}$, $F3_{NCS}$, $F4_{NCS}$, and $F1_{NCS}$), which are supposed to emerge between −85 ppm and −120 ppm (Table S5), are not discernible. Indeed, this can be explained by the large chemical shift anisotropy (CSA). From simulations of ^{19}F MAS NMR spectrum of NCS $KNaNbOF_5$ (Fig. 4), the obtained CSA of $F5_{NCS}$ is only 29.7 kHz, whereas the summed CSA of the equatorial fluorine atoms, $F2_{NCS}$, $F3_{NCS}$, $F4_{NCS}$, and $F1_{NCS}$, is 98.9 kHz. We attribute the poor sensitivity of the ^{19}F signals for $F2_{NCS}$, $F3_{NCS}$, $F4_{NCS}$, and $F1_{NCS}$ to both the slow spinning rate of 5 kHz and the relatively large CSA.

Upon heating NCS $KNaNbOF_5$ up to 450 °C, the ^{19}F NMR linewidth of the $F5_{NCS}$ signal remains unchanged. This temperature-independent line shape, which is consistent with our previous studies [39], indicates that there is no dynamic O/F disorder and the $[NbOF_5]^{2-}$ unit in the NCS phase experiences no axial rotations about the F_{apical}-Nb-O axis. Several additional features in the down-field spectra, however, emerge upon heating. At ∼360 °C, a ^{19}F peak at −143.2 ppm appears. We assign this peak to a phase associated with the reconstructive transition in the materials that is not related to its ferroelectric behavior; further details can be found in the Supplemental Material [42]. At 390 °C, the HT phase appears with a ^{19}F chemical shift at −116.7 ppm (Table S5). Upon further heating, fast axial rotations of the $[NbOF_5]^{2-}$ units occur, which gradually reduce the CSA of the equatorial fluoride anions and leads to an observable isotropic peak together with residual spinning side bands. This feature mirrors the growth of the HT phase in the irreversible reconstructive transition reported in Ref. [39] (Fig. S8), confirming the assignment of the −116.7 ppm resonance to the HT phase.

Additionally, another unknown ^{19}F peak at −114.8 ppm becomes visible at a higher temperature of 419 °C. Whether this ^{19}F signal suggests a new $KNaNbOF_5$ phase is currently under investigation. Overall, the evolution of the ^{19}F signals shown from −100 ppm to −160 ppm are reversible with temperature except for the peak associated with the reconstructive transition (Fig. S7), consistent with a second-order proper ferroelectric transition.

After *in situ* high-temperature ($T_{max} = 451$ °C) ^{19}F MAS NMR experiments, postmortem analysis on the heated NCS was investigated with ^{19}F MAS (25 kHz) NMR. Figure S9 shows that the ^{19}F resonances ($F1_{CS}$ and $F2_{CS}$) of the CS phase vanish from the pristine sample, leaving a clean signature of five ^{19}F signals ($F1_{NCS}$ to $F5_{NCS}$), which further support our previous findings [39]. This observation indicates that the CS phase converted to the NCS phase during the *in situ* high-temperature experiments. Finally, the chemical shifts of all ^{19}F signals in the NCS phase remain identical before/after the heat treatment ($T_{max} = 451$ °C). This means that the local environment of each fluorine atom in the NCS $KNaNbOF_5$ is unaltered, and therefore the $Pna2_1$-to-*Cmcm* transition is fully reversible.

D. Intermediate phase verification

We performed heating-and-quenching experiments on $KNaNbOF_5$ followed by ^{19}F NMR to identify the potential intermediate phases with *Pnna* and *Pnma* symmetry. First, we quenched (q) the $Pna2_1$ $KNaNbOF_5$ samples in ice bath after heating to the following select temperatures: $T_q = 360$ °C, 310 °C, 250 °C, and 150 °C. The quenched samples, denoted as for example $Pna2_1$(360 °C), were then studied with ^{19}F MAS (25 kHz) NMR. Figure 6(a) shows there are three characteristic ^{19}F signals, which correspond to the apical fluoride anions in the *Pnna* phase (−223.5 ppm), *Pnma* phase (−233.8 ppm), and $Pna2_1$ phase (−214.2 ppm). In contrast, the equatorial fluoride anions among the three phases manifest in broad and featureless ^{19}F resonances due to severe signal overlap from −80 ppm to −130 ppm (Table S5). The superimposed ^{19}F NMR peaks of the equatorial fluorides anions create a source of ambiguity in quantifying the individual phases. Therefore, we reference the phase fraction between

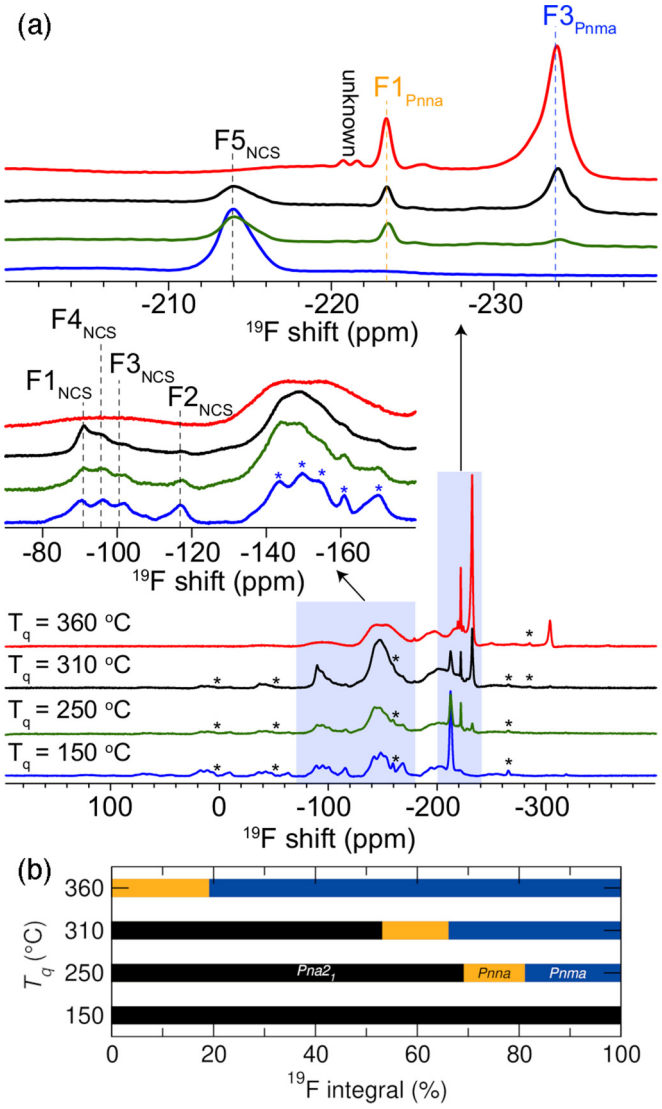

FIG. 6. (a) High-resolution ^{19}F MAS (25 kHz) NMR spectra of NCS $Pna2_1$ $KNaNbOF_5$ quenched (q) at $T_q = 150\,^{\circ}$C, 250 °C, 310 °C, and 360 °C. Asterisks * denote spinning side bands. (b) Phase fraction of $KNaNbOF_5$ phases found in the quenched samples at a given T_q, as determined by the phase fraction of the ^{19}F integral of the apical fluoride site. The black, yellow, and blue bars corresponds to the $Pna2_1$, *Pnna*, and *Pnma* phases, respectively.

intermediates (*Pnna* and *Pnma*) and the ending form of $KNaNbOF_5$ ($Pna2_1$) to the ^{19}F integral of the apical fluoride anions.

First, our quenching study reveals that quenching at lower temperatures leads to a greater phase fraction of the $Pna2_1$ phase compared to the intermediate phases (*Pnna* and *Pnma*) as show in Fig. 6(a). Specifically, when quenched from 360 °C, the *Pnma* phase consumed 81% of the total ^{19}F integral with the remaining 19% assigned to the *Pnna* phase [Fig. 6(b)]. At a lower quenching temperature of 310 °C, all three phases, *Pnna*, *Pnma*, and $Pna2_1$, were detected. The $Pna2_1$ phase grew and accounted for 53% of the total ^{19}F integral, whereas the ^{19}F integral of the *Pnna* and *Pnma* phases decreased from 19% to 13% (−6% reduction) and from 81% to 34% (−47% reduction), respectively. It should be noted that the overall loss of the intermediate phases is consistent with a transformation to the $Pna2_1$ phase. We observed a further increase (from 53% to 69%) of the $Pna2_1$ phase at the expense of the *Pnma* phase (from 34% to 19%) and the *Pnna* phase (from 13% to 12%) in the $T_q = 250\,^{\circ}$C samples [Fig. 6(b)]. Quenching the NCS phase at 150 °C resulted in the complete formation of the NCS $KNaNbOF_5$. This data allow us to conclude that the phase transition initiates at ≈250 °C and fully transforms to an intermediate structure at 360 °C. Additionally, we observe both intermediate phases from our symmetry analysis, *Pnma* and *Pnna*, occur experimentally.

The manner in which the ^{19}F integral varies among the apical fluoride anions ($F3_{Pnma}$, $F1_{Pnna}$, and $F5_{NCS}$) throughout the course of the quenching experiments suggests the energetic barrier between the *Pnma* and *Pnna* phases is low and thus, both phase transition pathways are possible. We also confirm that the *Pnna* phase results from the NCS to HT phase transition and not the contaminant perovskite-derived $P4/nmm$ phase in our sample by running equivalent quenching experiments on a $P4/nmm$ sample (Fig. S10). In the $P4/nmm$ quenching experiments, the *Pnna* phase does not appear until quenching at 370 °C in contrast to the NCS sample, which shows signatures of the *Pnna* phase at lower quenching temperatures. We therefore propose that the appearance of both the *Pnna* and *Pnma* phases in the NCS to HT phase transition is due both phases being accessible in the high-temperature potential energy landscape. The difference in energy between the relaxed phases is about 189 meV/f.u. with *Pnma* being the more stable (Fig. S4). If both phases are accessible, then we expect the lower-energy phase, *Pnma*, to be the majority phase with a small percentage of *Pnna* upon quenching the sample, as observed in our experiments.

We have confirmed that the displacive phase transition is reversible and consistent with previous measurements. By quenching the sample at various intermediate temperatures, we also confirm the existence of an intermediate phase, although its crystallographic symmetry remains to be determined as NMR is a technique that probes the short-range structural ordering. We also identify an additional high-temperature phase transition around 415 °C. Further attempts were made to determine the character of the phase transition through temperature-dependent second-harmonic generation (SHG) measurements, but due to the particular environmental conditions needed to keep the sample from degrading at high temperatures, we were unable to obtain reliable data at this time.

E. Electric polarization

Next, we computed the Berry phase polarization [50,51] and obtained 0.64 μC cm^{-2} along the c axis, which differs from the previously reported calculation of 0.21 μC cm^{-2} [52]. The value is small and reasonable as our analysis shows that the polarization in $KNaNbOF_5$ arises from the displacement of the anions. As seen in the structures of Fig. 7, the $[NbOF_5]^{2-}$ octahedra can be thought of as local ordered dipoles, which are aligned in an antipolar manner in the *Pnma* phase. Using a vector sum model [53], we calculate the dipole moment of the $[NbOF_5]^{2-}$ unit in the $Pna2_1$ phase as 1.9 debye, which is consistent with other heteroleptic polyhedra

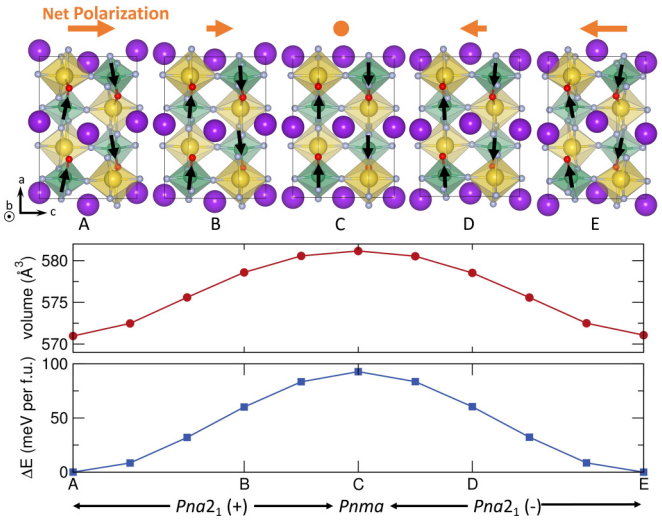

FIG. 7. Structure and properties along the minimum energy pathway for coherent monodomain polarization switching. The reaction coordinate is the total configurational change between images along the path. The letters correspond to structures along the switching pathway, shown above. The black arrows show the dipole moments of the $[NbOF_5]^{2-}$ octahedra and how their rotations contribute to the net polarization along the *c* axis (orange arrows).

[53,54] and only slightly smaller than the dipole of the unit in the *Pnma* phase (2.2 debye). This indicates that polarization is not enhanced by additional distortions to the local polar unit, $[NbOF_5]^{2-}$. As the atoms displace to lift inversion symmetry and produce the *Pna*2_1 structure, the octahedra rotate with opposite sense about the *b* axis in alternating rows along the *a* axis. This rotates the dipoles such that they are no longer compensated equally, and therefore sum to give a net polarization along the *c* axis analogous to weak ferromagnetism in canted antiferromagnets.

Although the calculated macroscopic polarization is small, we find both the electronic and ionic contributions to the polarization are large but of opposite signs, which is uncommon among simpler polar dielectrics. Using the Berry-phase method, we found the ionic and electronic polarizations were 2.63 μC cm^{-2} and -1.99 μC cm^{-2}, respectively. We confirmed these polarization values by calculating the polarization using a Wannier representation [55]. In this method, the Wannier functions of all occupied pairs of valence electrons are calculated, and because they are localized, their average positions or Wannier centers can be found. We then obtain the electric polarization as the sum of the ionic polarization (from displacements of atomic sites) and electronic polarization (from displacements of the Wannier centers). This analysis resulted in an electronic polarization of -1.99 μC cm^{-2} and total polarization of 0.64 μC cm^{-2}, which is identical to the result of the Berry-phase calculations. This significant contribution from the electronic polarization may be a common feature in heteroanionic materials, as this is also seen in calculations on $LaTiO_2N$, where the Berry-phase polarizations are twice as large as the point charge model [56].

The polarization in this compound arises from cooperative tilting of units with built-in dipoles, similar to heteroanionic materials with Λ-shaped units [10]. The cooperative tilts are likely driven by the bonding preferences of the K^+ ion as in oxide materials [57]. The global instability index (GII), a root-mean-squared error of the bond valence sum (BVS) compared to the nominal valence, is a measure of how ideal the cation-anion bonding is within a given crystal structure [58]. The GII of the proposed phase transition pathway (*Cmcm* to *Pnma* to *Pna*2_1) decreases, or becomes more ideal, through the transition. This decrease is primarily driven by the change in the BVS of the K^+ cation, which increases from 0.66 to 0.86 to 1.09 for the *Cmcm*, *Pnma*, and *Pna*2_1 phases, respectively. We also note that this mechanism is distinct from second-order Jahn-Teller induced ferroelectricity, as well as improper or hybrid improper mechanisms as the octahedra in the centrosymmetric structure already have second-order Jahn-Teller-like distortions, the polarization arises from a single soft mode, and the polarization does not originate from the uncompensated displacements of the A-site cations.

$KNaNbOF_5$ may be categorized as a proper geometric ferroelectric, however, there are some key differences between it and other geometric ferroelectrics. In *Pnma* $KNaNbOF_5$, the calculated born effective charges (Z^*, see Table S6) are slightly anomalous for the oxide and the fluoride anions that are not aligned with the black arrows in the structures in Fig. 7: $Z^*_{zz}(\mathrm{O}) = -0.83e$, $Z^*_{zz}(F4) = -1.89e$. This distinguishes it from proper ferroelectrics where the polarization is induced by the SOJT effect such as in $BaTiO_3$, which has very large anomalous charges ($Z^*(\mathrm{Ti}) = 7.3e$, $Z^*(\mathrm{O}_{||}) = -5.7e$ in its cubic structure [59]). In proper geometric ferroelectrics such as BaMF_4 (M = Mn, Fe, Co, Ni), the Born effective charges only deviate slightly from their nominal values and the electric polarization calculated either with the Berry-phase method or ionic-point charge model are in good agreement [60]. This agreement suggests the electronic contributions and enhanced covalency manifesting in large dynamical charges are minimal.

Although the Born effective charges are in good agreement with the nominal valences for the ions in $KNaNbOF_5$, as noted previously, the Berry-phase-calculated and ionic-model polarizations are significantly different. For that reason, it may not be deemed unambiguously as a geometric ferroelectric. Interestingly, the calculated polarization dependencies in $KNaNbOF_5$ are more similar to $HoMnO_3$ and other magnetically induced ferroelectrics, where the Born effective charges only slightly differ from their nominal values [$Z^*(\mathrm{Mn}) = 3.9e$, $Z^*(\mathrm{O}) = 3.1e$] and yet there is a difference between the electric polarization calculated from the ionic model and Berry-phase method, which accounts for both ionic and electronic contributions to the polarization [61]. There, the authors note that this large contribution of the electronic polarization is due to orbital polarization-induced charge polarization [62,63], which is not possible in $KNaNbOF_5$ as it is nonmagnetic. Further research into the polarization of $KNaNbOF_5$ and other heteroanionic materials with electronic polarizations should be pursued to clearly classify its ferroelectric mechanism.

F. Potential ferroelectric switching path

To investigate the feasibility of a switchable polarization in this compound, we calculate the energetics of a coherent

ferroelectric domain reversal or the monodomain switching barrier. Although this approach is a simple approximation of the ferroelectric switching mechanism, it provides a figure of merit that often indicates if polarization switching is possible. For example, the well-known ferroelectrics $PbTiO_3$ and $BaTiO_3$ have coherent energetic barriers of 50 meV/f.u. [64] and 16 meV/f.u. [65], respectively. If a material has a comparable barrier, then the polarization may likely be a switchable, but materials with significantly higher barriers are less likely to be ferroelectric and simply pyroelectric.

As noted previously, *Cmcm* has a large volume and energy difference relative to the ground-state structure, suggesting that if the transition were direct, the phase may not be switchable due to a large energetic barrier or potential cracking from a large strain gradient in the sample. The candidate intermediate phases, *Pnma* and *Pnna*, have an order of magnitude smaller volume change, and the energy difference to the $Pna2_1$ phase is also reduced, by up to about 300 meV/f.u. in the case of *Pnma* (Fig. S4). We therefore investigate a potential ferroelectric switching pathway through the *Pnma* phase, as is the lowest-energy intermediate phase and the most likely intermediate candidate based on the energetics of the singular modes.

To ensure an accurate modeling of the fluctuations in lattice parameters through the transition, we use a generalized solid-state nudged elastic band (G-SSNEB) calculation to model the monodomain switching. The results of the G-SSNEB, shown in Fig. 7, should predict the minimum energy pathway to switch the polarization of the material. The ferroelectric switching path through the *Pnma* structure proceeds smoothly along the minimum energy pathway. The maximum in both the volume and relative energy is at the CS intermediate and their values do not deviate much compared to their relaxed differences (Fig. S4). The maximum difference in energy is about 93 meV/f.u., which is about twice as large as the coherent energy switching barrier of $PbTiO_3$. However, we note that this value is comparable to other known ferroelectrics such as $LiNbO_3$ and $LiTaO_3$, which have barriers heights of around 130 and 65 meV/f.u., respectively [66]. Further investigations of the switching barrier height, either through 180° or 90° domain wall calculations or through two-step switching pathways [66–68] were outside the scope of this study, but may also lower the barrier height. We believe this suggests that the polarization may be switchable, but further investigation is needed to confirm the material is a ferroelectric. We attempted to measure the polarization hysteresis of $KNaNbOF_5$ under applied electric field, however due to the difficulty in sample processing, we were not able to confirm or refute its switchability.

IV. CONCLUSION

We have investigated the character of the NCS to HT CS phase transition in $KNaNbOF_5$ to gain insight into its potential switchable ferroelectricity. Using a Landau model constructed from DFT calculations of the relevant unstable modes, we determined that a direct transition was not possible, and an intermediate phase should appear between these known phases. We verified the existence of an intermediate phase through *in situ* and high-resolution ^{19}F MAS solid-state NMR, which suggested the intermediate phase to be *Pnma*, however, further long-range *in situ* structural characterization would be needed to prove this definitively. We also identified another high-temperature phase transition around 450 °C from the *Cmcm* phase to an unknown higher-temperature structure. Based on this proposed intermediate phase, we created a ferroelectric switching path and calculated its coherent energy switching barrier. Based on this simple metric, the material may be switchable as its energetic barrier is comparable to other known ferroelectrics. A hysteresis experiment would be necessary to confirm its switchability and we hope that our work sparks further experimental investigation into this material and other potential ferroelectric oxyfluorides. In addition, we showed that $KNaNbOF_5$, if switchable, is likely a proper ferroelectric rather than a hybrid improper as initially thought based on a symmetry analysis. Our combined theoretical and experimental approach can therefore be used to investigate the nature of ferroelectricity in other hybrid improper ferroelectrics. This will allow other researchers to verify the nature of ferroelectricity in other compounds as well.

ACKNOWLEDGMENTS

This work was supported by the National Science Foundation's MRSEC program (DMR-1720139) at the Materials Research Center of Northwestern University. H.L. acknowledges support from the National Science Foundation (NSF) under the Grant No. 1847038. Computational resources were provided by Carbon at the Center for Nanoscale Materials, an Office of Science user facility, was supported by the U.S. Department of Energy, Office of Science, Office of Basic Energy Sciences, under Contract No. DE-AC02-06CH11357 and the Extreme Science and Engineering Discovery Environment (XSEDE) Stampede2 at the University of Texas at Austin, which is supported by National Science Foundation Grant No. ACI-1548562. All solid-state NMR experiments were performed at the National High Magnetic Field Laboratory, which is supported by National Science Foundation Cooperative Agreement No. DMR-1644779 and the State of Florida. This work made use of the Jerome B.Cohen X-Ray Diffraction Facility supported by the MRSEC program of the National Science Foundation (DMR-1720139) at the Materials Research Center of Northwestern University and the Soft and Hybrid Nanotechnology Experimental (SHyNE) Resource (NSF ECCS-1542205). We acknowledge Zemp Yannik, Mads Weber, Thomas Loettermoser, and Manfred Fiebig for their efforts in performing and analyzing temperature-dependent SHG measurements.

[1] K. M. Rabe, M. Dawber, C. Lichtensteiger, C. H. Ahn, and J.-M. Triscone, Modern physics of ferroelectrics: Essential background, in *Phys. Ferroelectr.* (Springer, Berlin, 2007), pp. 1–30.

[2] P. S. Halasyamani and K. R. Poeppelmeier, Noncentrosymmetric oxides, Chem. Mater. **10**, 2753 (1998).

[3] J. M. Perez-Mato, P. Blaha, K. Schwarz, M. Aroyo, D. Orobengoa, I. Etxebarria, and A. García, Multiple instabilities in $Bi_4Ti_3O_{12}$: A ferroelectric beyond the soft-mode paradigm, Phys. Rev. B **77**, 184104 (2008).

[4] N. A. Benedek and C. J. Fennie, Hybrid Improper Ferroelectricity: A Mechanism for Controllable Polarization-Magnetization Coupling, Phys. Rev. Lett. **106**, 107204 (2011).

[5] J. M. Rondinelli and C. J. Fennie, Octahedral rotation-induced ferroelectricity in cation ordered perovskites, Adv. Mater. **24**, 1961 (2012).

[6] A. T. Mulder, N. A. Benedek, J. M. Rondinelli, and C. J. Fennie, Turning ABO_3 antiferroelectrics into ferroelectrics: Design rules for practical rotation-driven ferroelectricity in double perovskites and $A_3B_2O_7$ Ruddlesden-Popper compounds, Adv. Funct. Mater. **23**, 4810 (2013).

[7] K. Luo, R. D. Johnson, T. T. Tran, P. S. Halasyamani, P. G. Radaelli, and M. A. Hayward, $Ba_2YFeO_{5.5}$: A ferromagnetic pyroelectric phase prepared by topochemical oxidation, Chem. Mater. **25**, 1800 (2013).

[8] J. Young, E. J. Moon, D. Mukherjee, G. Stone, V. Gopalan, N. Alem, S. J. May, and J. M. Rondinelli, Polar oxides without inversion symmetry through vacancy and chemical order, J. Am. Chem. Soc. **139**, 2833 (2017).

[9] R. Gautier and K. R. Poeppelmeier, Preservation of chirality and polarity between chiral and polar building units in the solid state, Inorg. Chem. **51**, 10613 (2012).

[10] M. D. Donakowski, R. Gautier, J. Yeon, D. T. Moore, J. C. Nino, P. S. Halasyamani, and K. R. Poeppelmeier, The role of polar, lamdba (Λ)-shaped building units in noncentrosymmetric inorganic structures, J. Am. Chem. Soc. **134**, 7679 (2012).

[11] J. K. Harada, N. Charles, K. R. Poeppelmeier, and J. M. Rondinelli, Heteroanionic materials by design: Progress toward targeted properties, Adv. Mater. **31**, 1805295 (2019).

[12] D. Oka, Y. Hirose, H. Kamisaka, T. Fukumura, K. Sasa, S. Ishii, H. Matsuzaki, Y. Sato, Y. Ikuhara, and T. Hasegawa, Possible ferroelectricity in perovskite oxynitride $SrTaO_2N$ epitaxial thin films, Sci. Rep. **4**, 4987 (2015).

[13] S. Kikkawa, S. Sun, Y. Masubuchi, Y. Nagamine, and T. Shibahara, Ferroelectric response induced in *cis*-type anion ordered $SrTaO_2N$ oxynitride perovskite, Chem. Mater. **28**, 1312 (2016).

[14] G. Gou, M. Zhao, J. Shi, J. K. Harada, and J. M. Rondinelli, Anion ordered and ferroelectric ruddlesden-popper oxynitride $Ca_3Nb_2N_2O_5$ for visible-light-active photocatalysis, Chem. Mater. **32**, 2815 (2020).

[15] F. J. Brink, L. Norén, D. J. Goossens, R. L. Withers, Y. Liu, and C.-N. N. Xu, A combined diffraction (XRD, electron and neutron) and electrical study of $Na_3MoO_3F_3$, J. Solid State Chem. **174**, 450 (2003).

[16] J. F. Scott, Ferroelectrics go bananas, J. Phys.: Condens. Matter **20**, 021001 (2008).

[17] Z. Tylczyński, A collection of 505 papers on false or unconfirmed ferroelectric properties in single crystals, ceramics and polymers, Front. Phys. **14**, 63301 (2019).

[18] M. R. Marvel, J. Lesage, J. Baek, P. S. Halasyamani, C. L. Stern, and K. R. Poeppelmeier, Cation-anion interactions and polar structures in the solid state, J. Am. Chem. Soc. **129**, 13963 (2007).

[19] K. B. Chang, A. Vinokur, R. A. F. Pinlac, M. R. Suchomel, M. R. Marvel, and K. R. Poeppelmeier, How Lewis acidity of the cationic framework affects $KNaNbOF_5$ polymorphism, Inorg. Chem. **53**, 6979 (2014).

[20] R. A. F. Pinlac, C. L. Stern, and K. R. Poeppelmeier, New layered oxide-fluoride perovskites: $KNaNbOF_5$ and $KNaMO_2F_4$ ($M = Mo^{6+}, W^{6+}$), Crystals **1**, 3 (2011).

[21] A. D. Vasiliev and N. M. Laptash, Polymorphism of $KNaNbOF_5$ crystals, J. Struct. Chem. **53**, 902 (2012).

[22] M. Holland, N. Charles, J. M. Rondinelli, and K. R. Poeppelmeier, Reconstructive transitions from rotations of rigid heteroanionic polyhedra, J. Am. Chem. Soc. **138**, 11882 (2016).

[23] U. Petralanda and I. Etxebarria, Structural instabilities and sequence of phase transitions in $SrBi_2Nb_2O_9$ and $SrBi_2Ta_2O_9$ from first principles and Monte Carlo simulations, Phys. Rev. B **91**, 184106 (2015).

[24] C. A. L. Dixon, J. A. McNulty, K. S. Knight, A. S. Gibbs, and P. Lightfoot, Phase transition behavior of the layered perovskite $CsBi_{0.6}La_{0.4}Nb_2O_7$: A hybrid improper ferroelectric, Crystals **7**, 135 (2017).

[25] A. Tressaud and K. R. Poeppelmeier (eds.), *Photonic Electron. Prop. Fluoride Mater.* (Elsevier, Amsterdam, 2016).

[26] H. Kageyama, K. Hayashi, K. Maeda, J. P. Attfield, Z. Hiroi, J. M. Rondinelli, and K. R. Poeppelmeier, Expanding frontiers in materials chemistry and physics with multiple anions, Nat. Commun. **9**, 772 (2018).

[27] G. Kresse and J. Furthmüller, Efficient iterative schemes for *ab initio* total-energy calculations using a plane-wave basis set, Phys. Rev. B **54**, 11169 (1996).

[28] G. Kresse and J. Furthmüller, Efficiency of *ab-initio* total energy calculations for metals and semiconductors using a plane-wave basis set, Comput. Mater. Sci. **6**, 15 (1996).

[29] J. P. Perdew, A. Ruzsinszky, G. I. Csonka, O. A. Vydrov, G. E. Scuseria, L. A. Constantin, X. Zhou, and K. Burke, Restoring the Density-Gradient Expansion for Exchange in Solids and Surfaces, Phys. Rev. Lett. **100**, 136406 (2008).

[30] J. Sun, A. Ruzsinszky, and J. P. Perdew, Strongly Constrained and Appropriately Normed Semilocal Density Functional, Phys. Rev. Lett. **115**, 036402 (2015).

[31] N. Charles and J. M. Rondinelli, Assessing exchange-correlation functional performance for structure and property predictions of oxyfluoride compounds from first principles, Phys. Rev. B **94**, 174108 (2016).

[32] P. E. Blöchl, Projector augmented-wave method, Phys. Rev. B **50**, 17953 (1994).

[33] H. J. Monkhorst and J. D. Pack, Special points for Brillouin-zone integrations, Phys. Rev. B **13**, 5188 (1976).

[34] D. Sheppard, P. Xiao, W. Chemelewski, D. D. Johnson, and G. Henkelman, A generalized solid-state nudged elastic band method, J. Chem. Phys. **136**, 74103 (2012).

[35] A. Togo and I. Tanaka, First principles phonon calculations in materials science, Scr. Mater. **108**, 1 (2015).

[36] A. A. Mostofi, J. R. Yates, G. Pizzi, Y. S. Lee, I. Souza, D. Vanderbilt, and N. Marzari, An updated version of wannier90: A tool for obtaining maximally-localised Wannier functions, Comput. Phys. Commun. **185**, 2309 (2014).

[37] C. J. Pickard and F. Mauri, All-electron magnetic response with pseudopotentials: NMR chemical shifts, Phys. Rev. B **63**, 245101 (2001).

[38] J. R. Yates, C. J. Pickard, and F. Mauri, Calculation of NMR chemical shifts for extended systems using ultrasoft pseudopotentials, Phys. Rev. B **76**, 024401 (2007).

[39] P.-H. Chien, J. K. Harada, H. Liu, S. Patel, C. Huang, J. M. Rondinelli, K. R. Poeppelmeier, and Y.-Y. Hu, Microscopic insights into the reconstructive phase transition of $KNaNbOF_5$ with ^{19}F NMR Spectroscopy, Chem. Mater. **32**, 5715 (2020).

[40] B. J. Campbell, H. T. Stokes, D. E. Tanner, and D. M. Hatch, ISODISPLACE: A web-based tool for exploring structural distortions, J. Appl. Crystallogr. **39**, 607 (2006).

[41] D. M. Hatch and H. T. Stokes, INVARIANTS: Program for obtaining a list of invariant polynomials of the order-parameter components associated with irreducible representations of a space group, J. Appl. Crystallogr. **36**, 951 (2003).

[42] See Supplemental Material at http://link.aps.org/supplemental/10.1103/PhysRevMaterials.5.124401 for the details on the linear combination of eigenvectors; energy, volume, and structural details of all the phases of $KNaNbOF_5$; Landau coefficients and phase diagrams; DFT calculated ^{19}F NMR isotropic shifts and further ^{19}F NMR measurements on various $KNaNbOF_5$ phases; and born effective.

[43] E. B. Segal, First aid for a unique acid, HF: A sequel, Chem. Heal. Saf. **7**, 18 (2000).

[44] D. Peters and R. Miethchen, Symptoms and treatment of hydrogen fluoride injuries, J. Fluor. Chem. **79**, 161 (1996).

[45] J. C. Bertolini, Hydrofluoric acid: A review of toxicity, J. Emerg. Med. **10**, 163 (1992).

[46] W. T. A. Harrison, T. M. Nenoff, T. E. Gier, and G. D. Stucky, Tetrahedral-atom 3-ring groupings in 1-dimensional inorganic chains: Beryllium arsenate hydroxide hydrate ($Be_2AsO_4OH{\cdot}4H_2O$) and sodium zinc hydroxide phosphate hydrate ($Na_2ZnPO_4OH{\cdot}7H_2O$), Inorg. Chem. **32**, 2437 (2005).

[47] H. Ernst, D. Freude, T. Mildner, and I. Wolf, Laser-supported high-temperature MAS NMR for time-resolved in situ studies of reaction steps in heterogeneous catalysis, Solid State Nucl. Magn. Reson. **6**, 147 (1996).

[48] D. Orobengoa, C. Capillas, M. I. Aroyo, and J. M. Perez-Mato, AMPLIMODES: Symmetry-mode analysis on the Bilbao Crystallographic Server, J. Appl. Crystallogr. **42**, 820 (2009).

[49] J. M. Perez-Mato, D. Orobengoa, and M. I. Aroyo, Mode crystallography of distorted structures, Acta Crystallogr. Sec. A Found. Crystallogr. **66**, 558 (2010).

[50] N. A. Spaldin, A beginner's guide to the modern theory of polarization, J. Solid State Chem. **195**, 2 (2012).

[51] R. D. King-Smith and D. Vanderbilt, Theory of polarization of crystalline solids, Phys. Rev. B **47**, 1651 (1993).

[52] A. K. Mishra, M. R. Marvel, K. R. Poeppelmeier, and U. V. Waghmare, Competing cation-anion interactions and noncentrosymmetry in metal oxide-fluorides: A first-principles theoretical study, Cryst. Growth Des. **14**, 131 (2014).

[53] P. A. Maggard, T. S. Nault, C. L. Stern, and K. R. Poeppelmeier, Alignment of acentric $MoO_3F_3^{3-}$ anions in a polar material: $(Ag_3MoO_3F_3)(Ag_3MoO_4)Cl$, J. Solid State Chem. **175**, 27 (2003).

[54] H. K. Izumi, J. E. Kirsch, C. L. Stern, and K. R. Poeppelmeier, Examining the out-of-center distortion in the $[NbOF_5]^{2-}$ anion, Inorg. Chem. **44**, 884 (2005).

[55] Y. Noel, C. M. Zicovich-Wilson, B. Civalleri, P. D'Arco, and R. Dovesi, Polarization properties of ZnO and BeO: An *ab initio* study through the Berry phase and Wannier functions approaches, Phys. Rev. B **65**, 014111 (2002).

[56] N. Vonrüti and U. Aschauer, Anion Order and Spontaneous Polarization in $LaTiO_2N$ Oxynitride Thin Films, Phys. Rev. Lett. **120**, 046001 (2018).

[57] N. A. Benedek and C. J. Fennie, Why are there so few perovskite ferroelectrics? J. Phys. Chem. C **117**, 13339 (2013).

[58] I. D. Brown, Chemical and steric constraints in inorganic solids, Acta Crystallogr. Sect. B: Struct. Sci. **48**, 553 (1992).

[59] P. H. Ghosez, X. Gonze, and J. P. Michenaud, Lattice dynamics and ferroelectric instability of barium titanate, Ferroelectrics **194**, 39 (1997).

[60] C. Ederer and N. A. Spaldin, Origin of ferroelectricity in the multiferroic barium fluorides $BaMF_4$: A first principles study, Phys. Rev. B **74**, 024102 (2006).

[61] S. Picozzi, K. Yamauchi, B. Sanyal, I. A. Sergienko, and E. Dagotto, Dual Nature of Improper Ferroelectricity in a Magnetoelectric Multiferroic, Phys. Rev. Lett. **99**, 227201 (2007).

[62] H. Katsura, N. Nagaosa, and A. V. Balatsky, Spin Current and Magnetoelectric Effect in Noncollinear Magnets, Phys. Rev. Lett. **95**, 057205 (2005).

[63] C. Jia, S. Onoda, N. Nagaosa, and J. H. Han, Bond electronic polarization induced by spin, Phys. Rev. B **74**, 224444 (2006).

[64] S. P. Beckman, X. Wang, K. M. Rabe, and D. Vanderbilt, Ideal barriers to polarization reversal and domain-wall motion in strained ferroelectric thin films, Phys. Rev. B **79**, 144124 (2009).

[65] R. E. Cohen, Origin of ferroelectricity in perovskite oxides, Nature (London) **358**, 136 (1992).

[66] M. Ye and D. Vanderbilt, Ferroelectricity in corundum derivatives, Phys. Rev. B **93**, 134303 (2016).

[67] J. T. Heron, J. L. Bosse, Q. He, Y. Gao, M. Trassin, L. Ye, J. D. Clarkson, C. Wang, J. Liu, S. Salahuddin, D. C. Ralph, D. G. Schlom, J. Íñiguez, B. D. Huey, and R. Ramesh, Deterministic switching of ferromagnetism at room temperature using an electric field, Nature (London) **516**, 370 (2014).

[68] X. Z. Lu and J. M. Rondinelli, Room temperature electric-field control of magnetism in layered oxides with cation order, Adv. Funct. Mater. **27**, 1604312 (2017).